Infrared and Raman studies of the dead grain-boundary layers in SrTiO$_3$ fine-grain ceramics

Infrared and Raman studies of the dead grain-boundary layers in SrTiO₃ fine-grain ceramics

J Petzelt[1], **T Ostapchuk**[1], **I Gregora**[1], **P Kuzel**[1], **J Liu**[2] **and Z Shen**[2]

[1] Institute of Physics, Academy of Sciences of the Czech Republic, Na Slovance 2, 182 21 Praha 8, Czech Republic
[2] Department of Inorganic Chemistry, Stockholm University, SE-10691 Stockholm, Sweden

E-mail: petzelt@fzu.cz

Abstract

Infrared reflectivity, terahertz and Raman spectroscopy studies were carried out with two types of SrTiO₃ ceramic of mean grain size 1500 and 150 nm, and the results were compared with single-crystal data. Strong ferroelectric soft-mode stiffening was detected in the infrared data upon the decrease of the grain size, fully compatible with the reduction of the low-frequency permittivity in the whole temperature range 300–10 K. Weaker stiffening of this mode observed in the Raman spectra is explained by the higher phonon wavevector active in the Raman response and by a different geometry of its propagation. Raman data also confirmed a smaller tetragonality below the structural phase transition as compared to single crystals. This is explained by a special topology of tetragonal domains along the grain boundaries, in which the tetragonal axes are oriented perpendicularly to them. Broad low-frequency and low-temperature features in the Raman spectra are assigned to the smeared first-order ferroelectric soft-mode response from the polarized regions (∼3 nm thick) with reduced permittivity attached to the very narrow grain boundaries. Such an effect is caused by a local frozen polarization of mean value ∼15 μC cm^{-2} tending perpendicular to the grain boundary. To account for the full permittivity size effect, the grain boundary itself is modelled by a very thin (∼1 nm) dead layer with a strongly reduced local permittivity (∼8). The microscopic origin of the narrow dead layer is apparently a strong oxygen deficit, as suggested from recent local experiments and first-principles calculations by other authors. Coupling between the E-components of the ferroelectric and structural soft-mode doublets observed in the Raman spectra is due to the propagation of the E-symmetry polaritons through the polar grain boundaries, whereas the non-coupled A-symmetry polaritons are localized inside the non-polar grain bulk. Since the structurally disordered grain boundaries are very narrow, taking up only a very small volume fraction, their effect on the relaxation of the phonon momentum conservation can be neglected.

(Some figures in this article are in colour only in the electronic version)

1. Introduction

The problem of reduced dielectric response in granular high-permittivity materials (ceramics, polycrystalline films) compared to that in single crystals was revealed in several compounds as classical ferroelectric BaTiO$_3$ [1–5], incipient ferroelectric SrTiO$_3$ (STO) [6–9], relaxor ferroelectric PbMg$_{1/3}$Nb$_{2/3}$O$_3$ (PMN) and PMN–PT [10] and seems to be of general nature. In most of the studied cases it can be interpreted by the appearance of a thin (several nanometres thick) grain-boundary layer of substantially reduced permittivity, the so called dead layer. We have recently shown [9] that such a dead layer explains quite well the dielectric as well as infrared (IR) data of STO ceramics independent of the grain size and temperature. However, using the dead-layer model it is not possible to determine the layer thickness and permittivity independently; only their ratio can be fitted from the experimental data. Moreover, the microscopic nature of such layers has hardly been addressed yet. In the case of STO ceramics, based on the appearance of forbidden IR modes in the Raman spectra, it was suggested [7] that a frozen dipole moment develops in the grain boundaries, which might be the source of the dead layers. The picture of dead layers has also been recently supported by our dielectric, infrared and Raman study of STO fine-grain ceramics with the mean grain size of 150 nm: the first results were reported in [9]. In this paper we present complete results of this study and suggest a more quantitative picture of the dead layers based on a careful evaluation of our Raman data and recent local experiments and calculations: spatially resolved valence-electron energy-loss spectroscopy on the grain boundaries in bicrystals by van Benthem *et al* [11] and first-principles calculations and transport experiments by Shao *et al* [12].

2. Experiment and data evaluation

Our studies were performed on undoped and dense ceramics of 1500 and 150 nm average grain size, which we will refer to below as coarse-grain (CG) and fine-grain ceramics (FG), and on an undoped STO single crystal (SC) for comparison. The preparation and properties of the CG ceramics of 98.8% density were reported in [7]. Two fine-grain samples of 98% (FG*) and 99% (FG) density were consolidated by spark-plasma sintering [13]. The SEM image of FG ceramics is shown in figure 1.

The dielectric properties of both FG ceramics were measured using a 4192 LF Hewlett-Packard impedance analyser in the 10^2–10^6 Hz frequency range. IR reflectivity measurements were performed by a Bruker 113v Fourier transform IR (FTIR) interferometer with the resolution of 2 cm^{-1} in the 30–650 cm^{-1} range, using He-flow cryostats down to 10 K. FTIR data were complemented by the low-temperature transmission at 6–12 cm^{-1} on the thin (40 μm thick) platelet of FG* and power reflectivity at 30–40 cm^{-1} on FG using a monochromatic submillimetre spectrometer with coherent backward-wave-oscillator (BWO) sources. FTIR and BWO data were fitted with the factorized damped harmonic oscillator model [14] in order to obtain the complex dielectric response function of the polar lattice modes.

Raman scattering spectra of SC, CG and FG ceramics were measured in backscattering geometry using a Raman microscope (Renishaw RM 1000) equipped with a grating filter (NE*x*T) to enable measurements of Raman shifts as low as 10 cm^{-1}. The samples were placed in a continuous-flow He cryostat (Oxford Instruments Microstat) coupled to a Raman microscope by means of a special macro adapter. An Ar-laser line (514 nm) was used for excitation, with a spot diameter of $\sim$2 μm focused a few micrometres below the sample surface.

The Raman spectra of all three samples were taken in the range of 10–840 cm^{-1} under identical conditions at several temperatures from 5 to 300 K. To compensate for differences in overall scattering intensity due to different samples (scattering on grain boundaries) and to
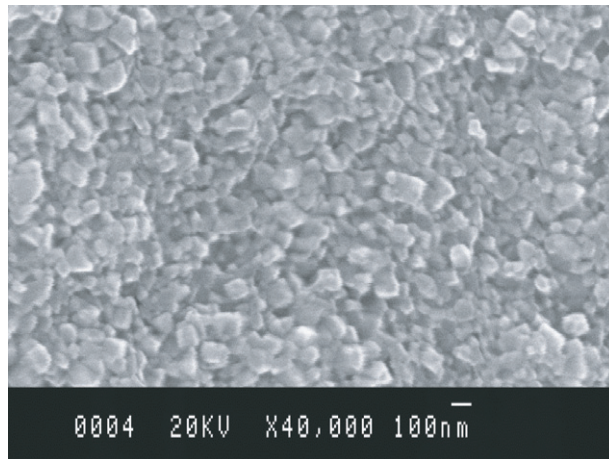
Figure 1. SEM image of FG ceramics. The average grain size is estimated to be 150 nm.

alignment errors, the Raman spectra were normalized so as to have the same integral intensity in the 570–840 cm^{-1} range. The normalized spectra were then carefully fitted in the range from 14 to 600 cm^{-1} by a sum of harmonic oscillators multiplied by the corresponding single-phonon temperature factor. The Rayleigh scattering tail at low frequencies was modelled by a temperature-independent zero-centred mixed Gaussian–Lorentzian peak (instrumental function) with a fixed width. We note that most of the spectral intensity in STO, in particular at higher temperatures, is due to second-order scattering, since the first-order scattering is forbidden in cubic STO single crystals. In this sense the harmonic oscillators used in the fits of second-order features do not have a straightforward physical interpretation: they represent a convenient, albeit fairly arbitrary, means of describing the broad background scattering of mainly two-phonon (or grain-boundary in the low-frequency range—see below) origin. In this way, we believe, we are able to obtain from the raw spectra reliable data characterizing the temperature evolution of the parameters of one-phonon spectral peaks and we could compare their intensities as well as the background intensity in all three types of STO samples.

3. Results

In figure 2 we present the temperature dependence of the dielectric permittivity of both FG and FG* ceramics compared with the CG one, taken from [7]. The reduction of the grain size from 1500 to 150 nm results in a very strong decrease in the low-temperature permittivity (about tenfold). The porosity of FG* induces a further decrease in the permittivity [15], but as long as we study high-density samples and assume closed-type porosity, the latter effect is negligibly small (of the order of several tens [15]). No appreciable dispersion was observed in either of the samples in the whole 10^2–10^6 Hz range at any temperature.

FTIR and BWO data on ceramics for selected temperatures together with the fitting curves are shown in figure 3. Note that the wavenumbers below 150 cm^{-1} are plotted in the logarithmic scale. The data on the CG ceramics are taken from [7]. BWO reflectivities of CG and FG* ceramics are calculated from the transmission and phase shift data on thin plane-parallel samples and the BWO reflectivity of the FG sample was measured directly in the 30–40 cm^{-1} range. Both FG and FG* ceramics exhibit slightly lower reflectivities than the CG sample.
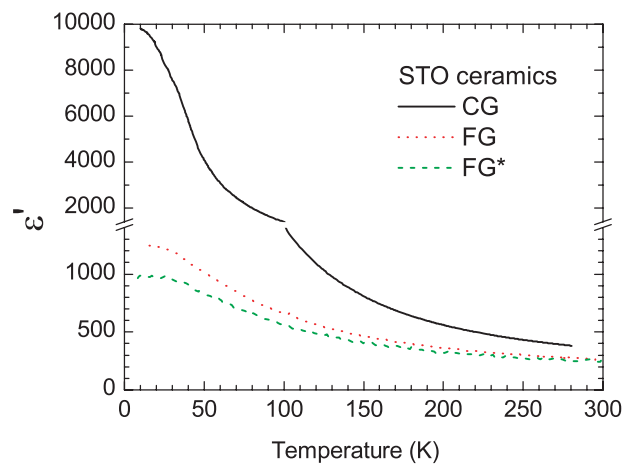
Figure 2. Temperature dependence of CG, FG, and FG* ceramic permittivity, measured at 10^2–10^6 Hz (no dielectric dispersion was observed in this frequency range).
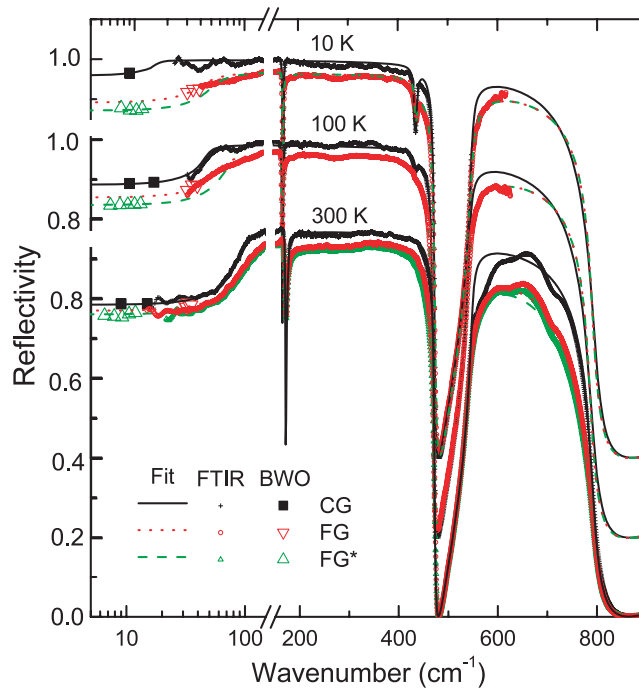

Figure 3. IR reflectivity (fitting curves, FTIR and BWO data) of CG, FG and FG* ceramics at selected temperatures.

This difference increases on cooling in the low-frequency part of the spectra, indicating the difference in the soft-mode behaviour.

Real and imaginary parts of the permittivity obtained from the fits to our reflectivity spectra are plotted in figure 4. Their low-frequency parts agree with the dielectric function calculated from the BWO measurements. For comparison, we added the dielectric spectra, obtained with a polycrystalline sol–gel film (thickness $\sim$ 360 nm) on sapphire substrate that
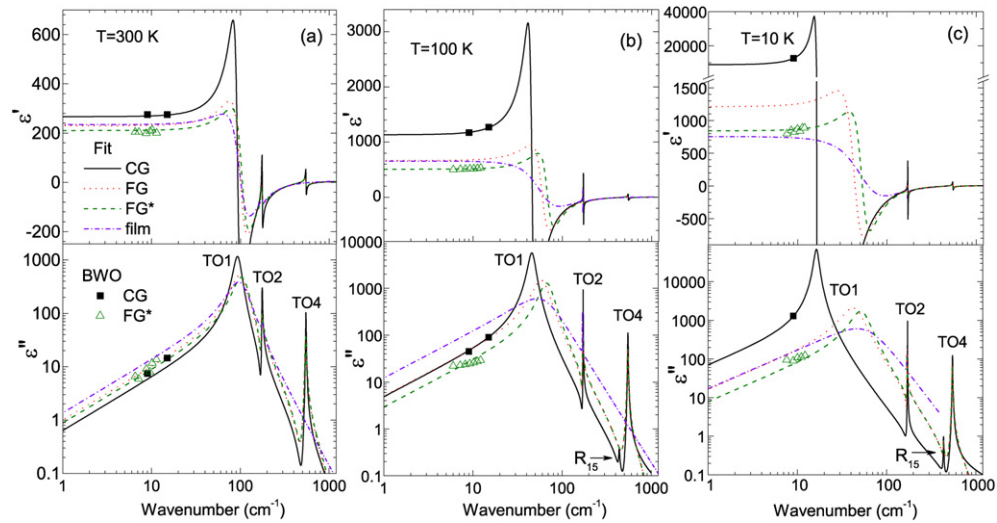
4

Figure 4. Real and imaginary parts of the complex dielectric function obtained from the fit to IR reflectivity of CG, FG, and FG* ceramics and IR transmission of the polycrystalline film [8] at 300 K (a), 100 K (b), and 10 K (c).

shows a comparable grain size, but cylindrical shape [8]. Reduction of the permittivity below the IR range in the FG sample compared with that in CG ceramics at the lowest temperature is in agreement with the low-frequency data (see figure 2). It is accounted for by an effective stiffening of the soft mode, which is comparable for all three samples with the sub-micrometre grain size. In addition, the soft-mode damping (width of the loss peak) also increases appreciably in the FG samples compared to that in CG ones. The response of the film is still much more smeared, apparently due to the film inhomogeneity. Temperature dependences of the ferroelectric soft-mode frequencies of these ceramics and film compared to those of SC are given in figure 5. The strong stiffening of the soft-mode frequencies at low temperatures in FG samples compared to that in CG ceramics and SC is fully compatible with the low-frequency permittivity data. No dielectric dispersion can therefore be expected below the soft-mode frequency range. Let us note that in [8] this effect in thin films was interpreted as due to possible nano-cracks along some of the grain boundaries. Only 0.2% of such crack-type porosity was sufficient to explain the soft-mode stiffening in comparison to SC. In fact, the nano-cracks were observed only in the thicker film (720 nm), where the stiffening was even more pronounced. In reality, one can expect a combination of both nano-cracks and dead-layer effects in our films. However, in our bulk ceramics the appearance of nano-cracks is not probable, since they remained compact and did not break upon polishing down to very small thicknesses (20–40 μm).

In figures 6(a)–(c), we present the temperature dependences of our Raman spectra of SC, CG, and FG ceramics, respectively, normalized as described in section 2 and reduced for the Bose–Einstein factor. The spectra are dominated by broad second-order bands around the 400 and 700 cm^{-1} range, which are well known and were assigned in the early studies on single crystals [16]. The assignment of sharper one-phonon peaks shown in the plots is based on that suggested in [7]. The temperature dependences of their frequencies in all three samples are shown in figure 7. The frequencies are evaluated from careful fits as described in section 2. An example of the fit along with the decomposition into individual damped-oscillator components
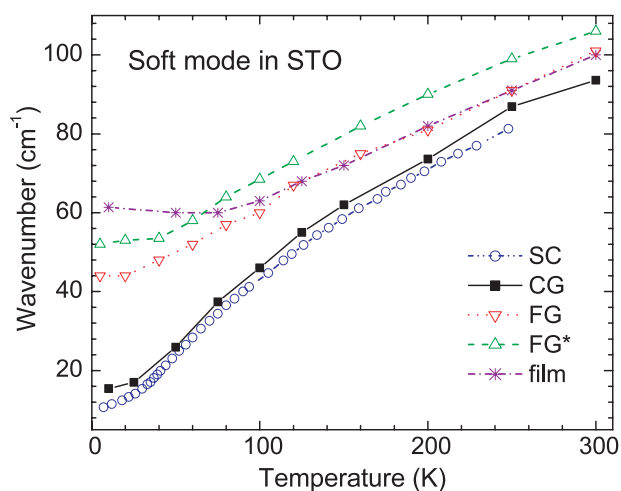
5

Figure 5. Soft-mode frequencies of STO SC, CG, FG, and FG* ceramics and polycrystalline film of the same grain size as FG ceramics.

is shown in figure 8. It is seen that in addition to one-phonon peaks a broad background appears, which differs at low temperatures for each sample. This is illustrated in figure 9, where the spectra of all the samples are compared for several low temperatures. The spectra are almost identical at high temperatures, but clearly differ below ∼100 K in the low-frequency range below ∼250 cm^{-1}.

In table 1 we summarize the measured phonon mode frequencies in both types of ceramics compared to SC at selected temperatures. Comparing results obtained from the Raman and IR spectra in different samples, we may conclude that significant differences are found for the two soft-mode doublets only.

4. Discussion

The measured IR and dielectric response indicates that in all our samples the dielectric dispersion below ∼5 THz is entirely due to the TO1 soft mode. The TO1 damping is much higher in the FG ceramics than in the other samples, particularly at low temperatures. Its oscillator strength (given by the product of its contribution to the permittivity $\Delta\varepsilon_s$ and the squared eigenfrequency ω_s^2) is essentially constant for all the samples and temperatures, $\Delta\varepsilon_s\omega_s^2 = (2.35 \pm 0.15) \times 10^6$ cm^{-2}, so that the variation in the low-frequency permittivity is fully due to the variation of the soft-mode frequency. This is expected since the generalized Lyddane–Sachs–Teller relation should be valid for the effective dielectric function of inhomogeneous media as well as of homogeneous ones. The generalized brick-wall model [22, 23], which holds for arbitrary grain shape and size within the approximation of an effective medium (i.e. homogeneous electric field in individual grains, sharp boundaries between the grain cores and thin shells), supports this result [24]. All higher-frequency polar phonons, including the longitudinal ones, are independent of the sample and temperature within the accuracy of our experiment (only their damping is slightly higher for the FG ceramics).

Concerning the Raman measurements, the spectra of ceramics differ from those of single crystals below the structural transition temperature. Note that this temperature somewhat differs for the CG ceramics (132 K) from that found in both SC and FG ceramics (∼107 K); the

Table 1. Phonon mode frequencies (in cm^{-1}) in CG and FG STO ceramics compared to the single crystal (SC). If the IR and Raman data differ or the mode is seen only in one type of spectra, the corresponding symbol (IR, R) is added in parentheses. Data on SC obtained in the present IR and Raman experiments are complemented by the results from the previous hyper-Raman [17, 18], Raman [19], neutron [20] and IR [21] studies. Missing data are indicated by dashes.

| Assignment	5 K			80 K			160 K			300 K		
	FG	CG	SC	FG	CG	SC	FG	CG	SC	FG	CG	SC
TO1(A$_{2u}$ + E$_u$)	23 (R) / 44 (IR)	18	8+17 [17]	39 (R) / 57 (IR)	40 (R) / 38 (IR)	40 (R) / 37 (IR)	62 (R) / 75 (IR)	63	58 (R) / 61 (IR)	101 (IR)	94 (IR)	90 (IR)
R$'_{15}$ E$_g$	34 (R)	41 (R)	15 [19]	—	—	12 [19]	—	—	—	—	—	—
R$'_{15}$ A$_g$	45 (R)	54 (R)	45 (R)	33 (R)	47 (R)	32 (R)	—	—	—	—	—	47 [20]
R$'_{25}$(B$_{1g}$ + E$_g$)	145 (R)	146 (R)	145 (R)	145 (R)	145 (R)	—	—	—	—	—	—	131 [20]
LO1(A$_{2u}$ + E$_u$)	170 (IR)	169 (IR)	170 (IR)	170 (IR)	170 (IR)	171 (IR)	170 (IR)	170 (IR)	171 (IR)	171 (IR)	171 (IR)	171 (IR)
TO2(A$_{2u}$ + E$_u$)	172	172	172	173	173	173 (IR)	173	173	173 (IR)	174	175 (IR)	173 (IR)
R$_{12}$(B$_{2g}$)	230 (R)	231 (R)	230 (R)	233 (R)	233 (R)	233 (R)	—	—	—	—	—	—
F$_{2u}$(TO3 + LO2) silent	266 (R)	264 (R)	264 (R)	265 (R)	265 (R)	—	—	—	—	—	—	266 [18]
R$_{15}$(E$_u$ − TO + LO)	437 (IR)	436 (IR)	439 (IR)	439 (IR)	439 (IR)	440 (IR)	—	—	—	—	—	—
R$'_{25}$(B$_{1g}$ + E$_g$)	449 (R)	449 (R)	449 (R)	447 (R)	447 (R)	449 (R)	—	—	—	—	—	426 [20]
LO3(A$_{2u}$ + E$_u$)	475 (IR)	474 (IR)	475 (IR)	475 (IR)	475 (IR)	475 (IR)	475 (IR)	475 (IR)	475 (IR)	474 (IR)	473 (IR)	474 (IR)
TO4(A$_{2u}$ + E$_u$)	550 (R) / 548 (IR)	548	546 (IR)	550 (R) / 544 (IR)	550 (R) / 544 (IR)	546 (IR)	550 (R) / 544 (IR)	545 (IR)	546 (IR)	544 (IR)	545 (IR)	542 (IR)
LO4 + R$_1$(A$_{2g}$)	—	795	788 [21]	—	796	790 [21]	—	796	790 [21]	790 (IR)	796	792 (IR)
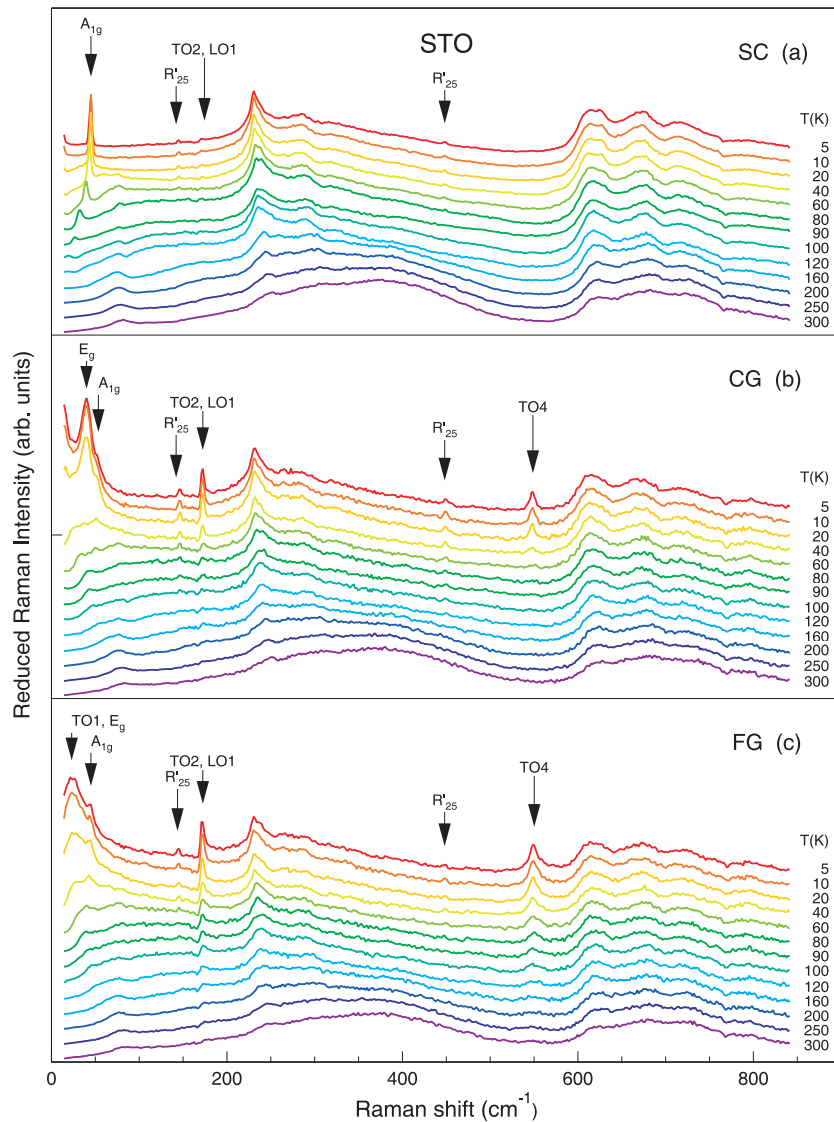
Figure 6. Temperature dependences of the reduced and normalized Raman spectra of STO samples: (a) SC, (b) CG, and (c) FG. For clarity, the spectra are equidistantly displaced vertically.

reason for this behaviour is not well understood. The relevant differences in the spectra concern particularly the TO1 frequency and the structural soft-mode doublet $E_g + A_{1g}$, but also some broad background features below 200 cm^{-1}, which are most pronounced in FG ceramics, less pronounced in CG ceramics, and still weaker (but not negligible) in SC (figure 9).

It is interesting to note that the Raman forbidden soft TO1 mode in SC starts to be discernible at temperatures as high as 160 K, emerging as a low-frequency shoulder on a two-phonon band at $\sim$80 cm^{-1}, in agreement with earlier studies [16]. On cooling, it further softens, crosses the A_{1g} soft mode at a temperature of $\sim$70 K and eventually merges with the Rayleigh wing, leaving a small but distinct trace of low-frequency inelastic scattering tail at the lowest temperatures (see figure 6(a)). Its Raman activity in SC is probably due to possible impurities
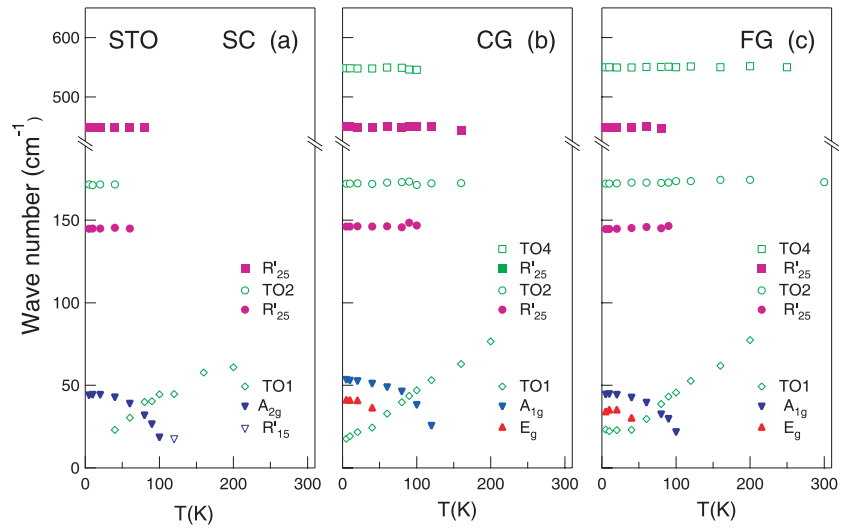
Figure 7. Frequencies of the assigned one-phonon peaks, obtained from the fits of Raman spectra: (a) SC, (b) CG, and (c) FG.
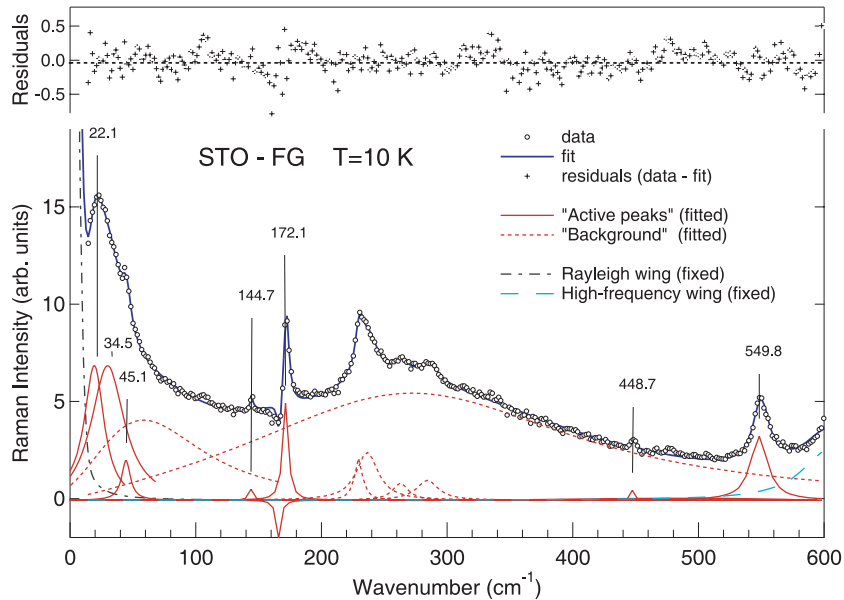

Figure 8. Example of the fit to normalized Raman spectra (FG sample at 10 K). Arrows indicate the fitted frequencies (in cm^{-1}) of the 'active' one-phonon peaks. The overall quality of the fit is illustrated by the residual curve in the upper part of the figure. Note that the negative oscillator peak at $\sim$167 cm^{-1} served to simulate the complex shape (antiresonance dip) of the TO2 peak at 172 cm^{-1} due to coupling effects.

and polar microregions, leading to partial activation of the TO1 soft branch away from the Γ point, as suggested in [25]. Hence, the respective Raman band becomes asymmetric at low temperatures, which may lead to overestimation of the TO1 frequency obtained from our oscillator fits.
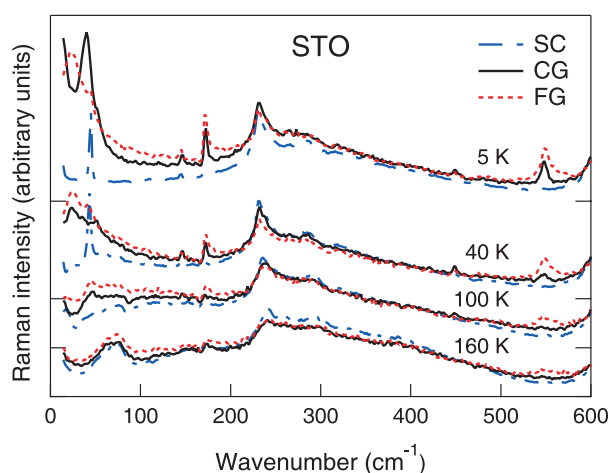
Figure 9. Raman spectra of SC, CG, and FG samples compared at several low temperatures.

The differences between the low-temperature TO1 frequencies obtained from the Raman spectra of FG ceramics and SC are much smaller than those deduced from the IR response. The soft-mode stiffening upon the decrease in the grain size, evaluated from the IR measurements, which fully accounts for the strongly reduced permittivity, can be quantitatively modelled by the depolarization field between the grain-boundary layers and the grain bulk within the effective medium approximation. However, an application of this approximation is not fully justified for the calculation of the Raman response, because the probing-field wavelength inside the FG ceramics does not significantly exceed the grain size; consequently, the electric field inside the individual grains is not homogeneous. Therefore, it is natural to expect a reduced stiffening of the Raman TO1 frequency as observed. It is important to stress that in such nano-inhomogeneous media the effective polar phonon frequencies observed in the Raman and IR response may substantially differ from each other due to the different wavevectors which couple with the probing electromagnetic wave fulfilling the momentum conservation. Here we assume that the momentum conservation is well satisfied in the crystalline grain bulk, which dominates over possibly essentially disordered but very thin grain boundaries. In fact, according to HRTEM studies on STO ceramics [26], a real grain boundary consists of well defined crystalline ($\Sigma = 3$) boundaries alternating on a nanoscopic scale with very thin amorphous boundaries. In all cases the structurally distorted boundaries are very thin, below 1 nm. Therefore, the integral volume of these boundaries even in our FG samples is quite small (in the 1% range of the total volume or less), so one can hardly expect any spectral features caused directly by them. Also, any effects of disorder (breaking of translational symmetry and of the momentum conservation) due to such thin boundaries and much larger crystalline grains can be safely neglected.

The behaviour of the structural soft-mode doublet confirmed our earlier interpretation in CG ceramics [7] that the TO1 mode strongly couples only with its E_g component, and that the A_{1g}–E_g splitting is much smaller in ceramic samples than in SC, indicating an order of magnitude smaller tetragonal distortion in both ceramic samples compared to the single crystal. The latter fact could be a consequence of mutual clamping of grains in the ceramics. The former fact (coupling of the E-components of the soft modes only) requires a closer discussion. The bilinear coupling between the polar and structural soft modes (E_u–E_g and A_{2u}–A_{1g}) is permitted in the grain boundary regions owing to the existence of the assumed polarization,

10

which removes the inversion centre. The results of recent *ab initio* calculations of the grain boundary structure in two STO bicrystals with 24° and 37° bicrystal misorientation [12] indicate that the grain boundary contains one charged oxygen vacancy per boundary unit cell and strongly deformed Ti–O and Sr–O pentagonal units which induce the tetragonal axis in the low-temperature perovskite lattice tending normal to the grain boundary. The dipole moment, which compensates the charged boundary, should be oriented perpendicularly to the boundary as well. Supporting this picture, a tremendous local decrease in the optical refractive index was observed around the grain-boundary regions with O vacancies [11].

A qualitative picture of the polariton mode behaviour near such a structure can be drawn from the point of view of the IR optics. We consider a thin barrier with a small permittivity (grain boundary) surrounded by a semi-infinite medium (grain bulk) with a very high permittivity. A low-permittivity layer has a repulsive character in optics, i.e. the rays always bend towards the higher-permittivity dielectric medium [27]. Phonon polaritons propagating approximately perpendicularly to the grain boundary (E-modes polarized perpendicularly to the tetragonal axis) are transmitted through the thin barrier and can be influenced by its properties. On the other hand, the field of p-polarized waves incident on the barrier under higher angles, which can be associated with the A-modes with the electric field polarization along the tetragonal axis, is not transmitted through the low-permittivity layer and can penetrate into the zone with non-vanishing polarization as evanescent waves only. This indicates that the E_u and E_g components can efficiently couple in the polarized grain-boundary regions, while the A_{2u} and A_{1g} components cannot, even if the resulting local polar 4 mm (C_{4v}) point group would allow for both couplings in an infinite crystal with such symmetry. The E-components have electric field predominantly parallel to the grain boundaries, where the depolarization field effect is minimized. This also explains the smaller stiffening of the E(TO1) frequency in the Raman spectra compared to that in the IR response, in which the boundaries normal to the E-mode electric field (connected with the maximum depolarization field) dominate due to much larger wavelength in the IR response.

The smaller tetragonality might be due to the fact that the grain boundaries induce the tetragonal phase below the structural transition with the tetragonal axis locally perpendicular to the boundary. Such deformation would produce structural singularities towards the grain centre, which could be partially avoided by much smaller deformation in the grain bulk. This feature deserves a careful structural study, which, to the best of the authors' knowledge, is not available on STO ceramics to date.

Concerning the broad background observed at low temperatures below about 200 cm^{-1}, we assign it to the first-order TO1 soft-mode response localized near grain boundaries and broad antiphase boundary regions [28]. Its smearing corresponds clearly to the expected large inhomogeneities in these regions. We can estimate the average local permittivity value in the grain-boundary regions from the Raman spectra assuming that the STO perovskite structure is preserved in these regions, the local permittivity decrease is entirely due to the modified soft-mode dynamics, and TO1 oscillator strength does not significantly differ from the bulk value. In this case the local permittivity is inversely proportional to the squared local soft-mode frequency: $\varepsilon_{gb} \propto 1/\omega_{\mathrm{TO1(gb)}}^2$.

To obtain a more quantitative estimate of the background part of the Raman spectra, we subtracted from the spectra all the fitted one-phonon lines (frequencies of these lines are plotted in figure 7). The background obtained after such a subtraction for low-temperature spectra is plotted in figure 10. It is seen that the background from ∼200 cm^{-1} down to the low-frequency limit of our measurements (15 cm^{-1}) becomes stronger in the CG ceramics and still stronger in the FG one, with the maximum near 70 cm^{-1}. This corresponds to local static permittivity variation from the bulk values down to ∼30 (corresponding to the local TO1
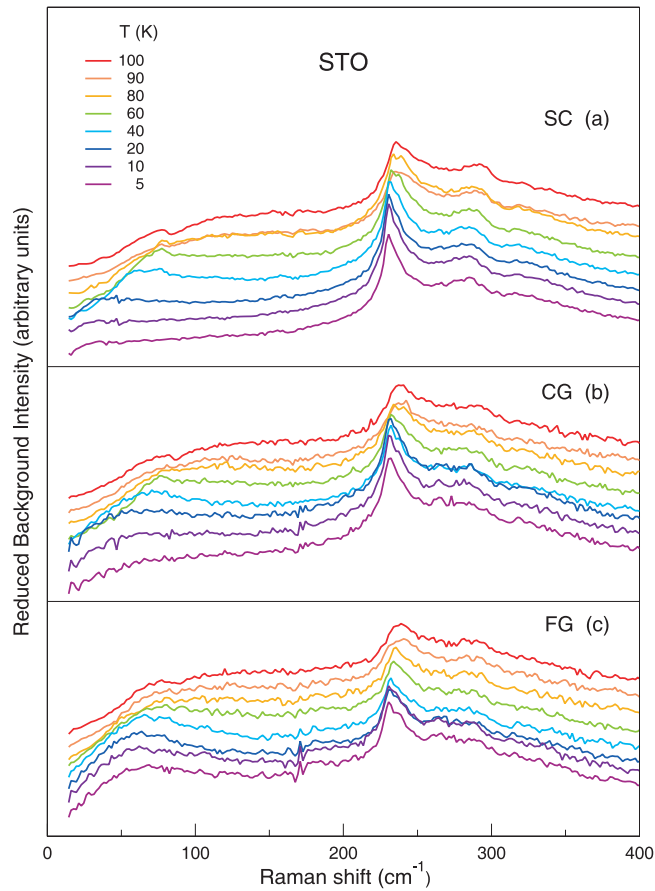
11

Figure 10. Temperature evolution of the 'background' part of the spectra (after subtraction of all the fitted one-phonon peaks) below 100 K: (a) SC, (b) CG, and (c) FG. For clarity, the spectra are equidistantly shifted upwards with increasing temperature.

frequency of 200 cm^{-1}), with the average value of $\sim$500 (corresponding to the local TO1 frequency of 70 cm^{-1}) at the lowest temperature. To account for the strongly reduced static effective permittivity (at 5 K the bulk value is about 25 000, CG ceramic yields about 10 000, and FG ceramic about 1000), we would need a homogeneous dead layer of thickness d and permittivity $\varepsilon_{\mathrm{gb}}$ fulfilling $\varepsilon_{\mathrm{gb}}/d \cong 10$ nm^{-1} [9]. Note that within this model (essentially a series capacitor model) it is impossible to determine the dead-layer permittivity and thickness separately. In our case, the equivalent homogeneous dead layers for the permittivity of 500 should be rather thick ($\sim$50 nm), which is far too much for a realistic estimate. Consequently, it appears that the model of a single homogeneous dead layer, which accounts well for the static data, is not fully appropriate for the discussion of the dynamic (particularly Raman) response.

It is more probable that the very thin grain-boundary layer, which is structurally different from the perovskite lattice [11, 12], has locally a very low permittivity. Indeed, the large soft-mode contribution is locally missing here because its eigenvector should include the lacking oxygen atoms. On the other hand, the broad features in the Raman response stem, in our opinion, from the perovskite lattice polarized (and only slightly deformed) by the charged grain boundaries, which might be several nanometres thick. In [7] we argued that the thickness

of such layers is given by the correlation length of the polarization fluctuations, which, in principle, can be determined from the Landau theory of the paraelectric STO. In [9], based on soft-mode dispersion data [29], we estimated this length to $\xi = 5.6$ nm at 5 K. However, this estimate neglects the anisotropy of the soft-phonon constant energy surface in the reciprocal space, which is quite pronounced [30], and the coupling of the soft branch with acoustic branches. Both these effects lead to a smaller value of ξ than the above estimate, but accurate numbers are not easily accessible.

We thus came to a model of a structured grain boundary composed of a very thin charged non-perovskite layer with a very low and temperature-independent local permittivity enclosed in somewhat thicker polarized layers with only slightly distorted perovskite structure. The effective thickness of the latter layers should be appreciably temperature dependent because the polarization correlation length fulfils the proportionality $\xi \propto \sqrt{\varepsilon}$ [7]. It then appears that at higher temperatures (above $\sim$100 K) the thin grain-boundary layer with very small local permittivity is dominant in the effective response, whereas at low temperatures both types of layers may become important.

Let us estimate more quantitative values of parameters for both suggested dead layers at low temperature using a simple brick double-wall model assuming cubic bricks in our FG ceramics—see figure 11. The effective permittivity for such a model is given by

$$\varepsilon_{\mathrm{eff}}^{-1} = V_{\mathrm{b}}\varepsilon_{\mathrm{b}}^{-1} + \tfrac{1}{3}V_{\mathrm{p}}\varepsilon_{\mathrm{p}}^{-1} + \tfrac{1}{3}V_{\mathrm{gb}}\varepsilon_{\mathrm{gb}}^{-1}, \tag{1}$$

where V_{b} and ε_{b} are the relative volume (concentration) and permittivity of the grain bulk, V_{p} and ε_{p} are the concentration and permittivity of the polarized layers, and V_{gb} and $\varepsilon_{\mathrm{gb}}$ are the concentration and permittivity of the thin grain-boundary layers, respectively. Clearly, $V_{\mathrm{b}} = 1 - V_{\mathrm{p}} - V_{\mathrm{gb}}$. Assuming at 10 K $\varepsilon_{\mathrm{b}} = 25\,000$, $\varepsilon_{\mathrm{p}} = 500$, $\varepsilon_{\mathrm{gb}} = 8, V_{\mathrm{p}} = 0.12$ ($\xi = 3$ nm, the thickness of the polarized region is 2ξ), and $V_{\mathrm{gb}} = 0.02$ ($d_{\mathrm{gb}} = 1$ nm), we obtain $\varepsilon_{\mathrm{eff}} = 1050$, in agreement with our experiment. The dominant effect is due to the thin grain-boundary layers, which alone reduce the effective permittivity to 1150. The effect of the polarized layer alone reduces the permittivity to 8680 only. At higher temperatures, ε_{p} and V_{p} should be smaller in our model, but the accuracy is not high enough to obtain reliable numbers for them. At higher temperatures, the effect of the polarized layers becomes negligible and the thin grain-boundary layers (with essentially temperature-independent parameters) dominate. By the effect of this layer only, the room-temperature permittivity of our FG ceramics is reduced from 300 to 244 and the TO1 frequency is stiffened from 90 to 100 cm^{-1}, in perfect agreement with our experiment. It is interesting to stress that the oxygen-deficit boundary also produces a very strong local reduction of the room-temperature optical refractive index [11], which surprisingly affects a broader region, more than 5 nm thick. This picture was confirmed by spectroscopic ellipsometric refractive-index measurements on our ceramics [9], yielding at $10\,000$ cm^{-1} $n = 2.25$ and 2.20 for the CG and FG ceramics, respectively, compared with $n = 2.4$ for SG.

The thin low-permittivity layer brings the leading contribution to the reduction of the static permittivity of the ceramics. The polarized layer is important at low temperatures only. It yields a small correction to the effective static permittivity and allows us to understand the activation of the IR modes in the Raman spectra, the broad low-frequency features and the observed coupling between the E-components of the soft-mode doublets (see figure 11(b)). Using our model, the behaviour of phonon polaritons near grain boundaries can be calculated more quantitatively. We use the transfer matrix formalism [27] to calculate the amplitude transmittances of electromagnetic waves corresponding to the relevant polariton frequencies and wavevectors through our model structure. For this simulation we assume that the layered grain boundary structure is an infinite plane interface (see figure 11(b)). We are aware that this
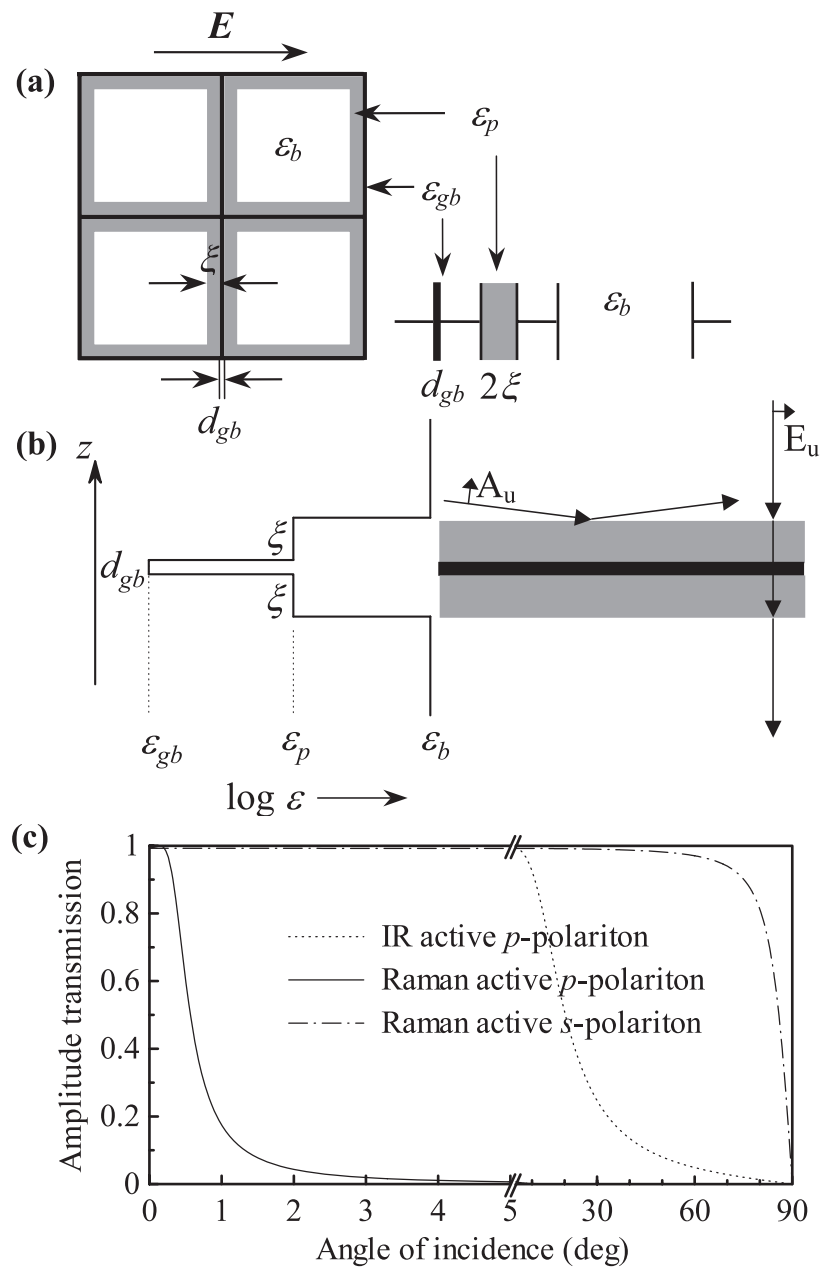
13

Figure 11. (a) Brick double-wall model and equivalent series capacitor circuit. (b) Scheme of the optical interface for the phonon polariton propagation. Between each grain core (white) with bulk properties (ε_b) there is one grain-boundary layer (black) with permittivity ε_{gb} and thickness d_{gb} and two polarized layers (grey) with permittivity ε_p and thickness ξ. (c) Amplitude transmission of *s*- and *p*-polarized electromagnetic waves incident on the grain-boundary structure versus angle of incidence.

approximation is not fully justified for calculation at the Raman active wavevectors; however, we deem that it provides a good qualitative picture. In figure 11(c) we plot the amplitude

transmission of *p*- and *s*-polarized electromagnetic waves incident on the layered structure as a function of the incidence angle. The results are shown for both Raman and far-IR active wavevectors of the polaritons. The *s* polarization and the angles of incidence close to 0° for the *p* polarization are related to the E_u-component of the soft mode (the electric field of the mode is normal to the tetragonal axis), while the grazing angles of incidence for the *p* polarization correspond to its A_{2u} component (electric field parallel to the tetragonal axis). Only evanescent fields penetrate into the grain-boundary layers for the *p*-polarized polaritons in the Raman regime for the incidence angles larger than about 1°.

Finally, let us estimate the average value of the frozen polarization in the polarized layers near the grain boundaries from the thermodynamic model. The lowest-order free-energy expansion in terms of the polarization vector (P_x, P_y, P_z) reads [28, 31]

$$
F(T) = \frac{1}{2(\varepsilon_b(T) - 1)} \left(P_x^2 + P_y^2 + P_z^2 \right) + \frac{1}{4}\beta \left(P_x^4 + P_y^4 + P_z^4 \right)
$$
$$
+ \tfrac{1}{2}\beta' \left(P_x^2 P_y^2 + P_y^2 P_z^2 + P_z^2 P_x^2 \right) \dots . \tag{2}
$$

In the experiment we probe the in-plane permittivity ε_p, while only the normal component of the polarization is non-zero. In this case the dielectric constant in the polarized layer reads

$$
\varepsilon_p = \frac{\varepsilon_b}{1 + \beta' \varepsilon_b \varepsilon_0 P_z^2}, \tag{3}
$$

where ε_0 is the vacuum permittivity. Taking into account the numerical values of the parameters in equation (3), $\varepsilon_b \approx 25\,000$, $\varepsilon_p \approx 500$, and $\beta' \sim 1 \times 10^{10}$ J C^{-4} m^5 [31], we find $P_z \approx 15\ \mu$C cm^{-2}, which compares well with the P_S value in BaTiO$_3$, for instance.

5. Conclusions

The IR reflectivity and Raman spectra of fine-grain (150 nm) STO ceramics were measured in the 300–10 K range and carefully compared with those of coarse-grain (1500 nm) ceramics and with a single crystal. The strong permittivity reduction with decreasing grain size is fully revealed in the effective ferroelectric soft-mode stiffening, seen in the IR spectra. However, the Raman response shows smaller stiffening, as expected owing to its higher wavevector (comparable with the reciprocal grain size) implied in the Raman response. Here we assume that according to previous HRTEM studies the grain boundaries are extremely thin and the grain bulk is well crystalline, so that the effects of broken translational symmetry on the phonon activity can be neglected. The Raman spectra also bring evidence of the coupling between the E_u component of the ferroelectric soft mode and the E_g component of the structural soft mode and of much smaller low-temperature tetragonality of the STO ceramics compared with single crystals. In this picture, the distorted grain boundaries induce the structural phase transition below 107 K in such a way that the tetragonal axis is forced to be locally oriented along the boundary normal. This effect presumably leads to a reduction of the average tetragonality rather than to a generation of a large number of structural defects in the grain bulk, which could be energetically more costly.

The Raman spectra of ceramics differ from those of a single crystal below ∼100 K in the low-frequency range, which, in addition to contributions from the bulk one-phonon scattering, reveals broad features assigned to a smeared TO1 phonon in strongly polarized regions near the grain boundaries. A rough estimate gives the mean permittivity $\varepsilon_p = 500$ in these regions at low temperatures. These layers are, however, not sufficient to explain the observed reduction of the static permittivity. An additional very thin layer (∼1 nm) with strongly reduced temperature-independent permittivity ($\varepsilon_{gb} = 8$) is needed to explain the data.

Such a layer originating in the oxygen deficit in grain boundaries was recently suggested by spatially resolved valence-electron energy-loss spectroscopy [11], transport properties and first-principles calculations [12].

Acknowledgments

References

[1] Arlt G, Hennings D and de With G 1985 *J. Appl. Phys.* **58** 1619
[2] Frey M H, Xu Z, Han P and Payne D 1998 *Ferroelectrics* **206** 337
[3] Polotai A V, Ragulya A V and Randall C A 2003 *Ferroelectrics* **288** 93
[4] Zhao Zh, Buscaglia V, Viviani M, Buscaglia M T, Mitoseriu L, Testino A, Nygren M, Johnsson M and Nanni P 2004 *Phys. Rev.* B **70** 024107
[5] Buscaglia M T *et al* 2006 *Phys. Rev.* B **73** 064114
[6] Li H Ch, Si W, West A D and Xi X X 1998 *Appl. Phys. Lett.* **73** 464
[7] Petzelt J *et al* 2001 *Phys. Rev.* B **64** 184111
[8] Ostapchuk T *et al* 2002 *Phys. Rev.* B **66** 235406
[9] Petzelt J, Ostapchuk T, Gregora I, Savinov M, Chvostova D, Liu J and Shen Zh 2006 *J. Eur. Ceram. Soc.* **26** 2855
[10] Carreaud J, Geimeiner P, Kiat J M, Dkhil B, Bogicevic C, Rojac T and Malic B 2005 *Phys. Rev.* B **72** 174115
[11] van Benthem K, Tan G, DeNoyer L K, French R H and Ruhle M 2004 *Phys. Rev. Lett.* **93** 227201
[12] Shao R, Chisholm M F, Duscher G and Bonnell D A 2005 *Phys. Rev. Lett.* **95** 197601
[13] Liu J, Shen Zh, Nygren M, Su B and Button T W 2006 *J. Am. Ceram. Soc.* **89** 2689
[14] Gervais F 1983 *Infrared and Millimeter Waves* vol 8, ed K J Button (New York: Academic) p 279
[15] Rychetsky I, Petzelt J and Ostapchuk T 2002 *Appl. Phys. Lett.* **81** 4224
[16] Nilsen W G and Skinner J G 1968 *J. Chem. Phys.* **48** 2240
[17] Yamanaka A, Kataoka M, Inaba Y, Inoue K, Hehlen B and Courtens E 2000 *Europhys. Lett.* **50** 688
[18] Vogt H and Neumann G 1979 *Phys. Status Solidi* b **92** 57
[19] Fleury P A, Scott J F and Worlock M 1968 *Phys. Rev. Lett.* **21** 16
[20] Stirling W G 1972 *J. Phys. C: Solid State Phys.* **5** 2711
[21] Kamaras K, Barth K-L, Henn R, Reedyk M, Thomsen C, Cardona M, Kircher J, Richards P L and Stehle J-L 1995 *J. Appl. Phys.* **78** 1235
[22] Rychetsky I and Petzelt J 2004 *Ferroelectrics* **303** 137
[23] Petzelt J and Rychetsky I 2005 *Ferroelectrics* **316** 89
[24] Rychetsky I 2005 private communication
[25] Uwe H, Yamaguchi H and Sakudo T 1989 *Ferroelectrics* **96** 123
[26] Ernst F, Kienzle O and Ruhle M 1999 *J. Eur. Ceram. Soc.* **19** 665
[27] Born M and Wolf E 2003 *Principles of Optics* 7th edn (Cambridge: University Press)
[28] Tagantsev A K, Courtens E and Arzel L 2001 *Phys. Rev.* B **64** 224107
[29] Shirane G and Yamada Y 1969 *Phys. Rev.* **177** 858
[30] Shirane G, Axe J D, Harada J and Linz A 1970 *Phys. Rev.* B **2** 3651
[31] Fleury P A and Worlock J M 1968 *Phys. Rev.* **174** 613